ChemComm

COMMUNICATION

View Article Online
View Journal | View Issue



Cite this: *Chem. Commun.*, 2025, **61**, 3331

Received 10th October 2024,
Accepted 27th January 2025

DOI: 10.1039/d4cc05351f

rsc.li/chemcomm

# Through-space conjugation driven luminescence enhancement in crystalline butterfly architectures†

Suvarna Sujilkumar, ‡[a] Avinash Hari ‡[b] and Mahesh Hariharan *[a]

**Through-space conjugation in organic chromophores offers significant potential for developing highly efficient luminescent materials. Herein, we investigate the luminescencent properties of crystalline tetra-naphthalene connected dihydropentacene isomers, 1-NP and 2-NP, using both experimental and theoretical approaches, establishing the presence of through-space conjugation mediated luminescence enhancement.**

Organic luminescent materials play a pivotal role in the development of optoelectronic devices, sensors, biological probes, and so on.[1–3] Understanding the fundamental principles and mechanisms accountable for the intriguing photophysical changes that occur in a chromophore, from its monomeric state to its aggregate state, is of great interest.[4,5] The pioneering work by Tang and co-workers on hexaphenylsilole paved the way for luminogens exhibiting aggregation-induced emission (AIEgens).[6] Through-bond conjugation (TBC) and/or through-space conjugation (TSC) possibly act as the key factors in determining the efficiency of luminogens by enabling effective electron delocalisation within the molecular scaffold.[7] AIE of conventional luminogens is well explained by TBC mediated rigidification and restriction of intramolecular motions (RIM), which enhances photoluminescence in both crystalline and aggregate states.[4,8] Apart from TBC, recent studies have emphasized the role of TSC, a non-bonding interaction arising from the spatial proximity of the orbitals, can assist in enhancing the luminescence, commonly observed in non-conjugated molecules upon formation of aggregates or crystals.[9,10]

Chromophores with low π-conjugation that exhibit visible-range emission are highly sought after due to their superior biocompatibility and processability compared to highly conjugated luminogens.[11] Previous reports have shown the presence of TSC in luminogens with limited π-conjugation.[12] Therefore, designing materials with low-conjugation structure and a through-space interacting molecular framework will facilitate the investigation of TSC effects. Dihydroacene derivatives, a group of cross-conjugated chromophores, can exhibit luminescence enhancement due to the interplay between multiple inter- and intramolecular interactions, coupled with the formation of a rigid contorted butterfly architecture resulting from the incorporation of bulky substituents.[13] The presence of AIE in dihydroacene derivatives is well explained *via* RIM mechanisms; however, the integral role of TSC remains less explored.[13] Herein, we explore the role of TSC in achieving enhanced luminescence using two positional isomers of tetra-naphthalene connected dihydropentacene derivatives, namely **1-NP** and **2-NP**.

**1-NP** and **2-NP** were synthesized and characterized according to the previously reported procedure (Schemes S1, S2 and Fig. S1, S2, ESI†).[14] Good quality single crystals of **1-NP** and **2-NP** were obtained by slow evaporation from a 1 : 1 chloroform-hexane mixture, respectively (Fig. 1, Fig. S3, S4 and Table S1, ESI†). The crystal structure of **1-NP** contains two chloroform molecules in the asymmetric unit. To unravel the nature and strength of various noncovalent interactions present in the crystalline architectures, Hirshfeld surface, truncated symmetry-adapted perturbation theory (SAPT(0)), and electrostatic surface potential (ESP) analysis were performed.[15,16] Hirshfeld surface analysis provides a quantitative picture of the role of weak intermolecular interactions in the crystal assembly. The generated Hirshfeld surface and the two-dimensional fingerprint plots revealed a high value of % C–H···C/% C···C (>4.5), indicating the dominant role of edge-face interactions in governing a herringbone-type crystal packing motif (Table S2 and Fig. S5, S6, ESI†). Closer inspection of the crystal packing revealed three types of dimers for **1-NP** and two types of dimers for **2-NP** (Fig. S7–S11, ESI†). SAPT(0) analysis elucidated a dispersion dominant stabilization exhibited by all the identified dimers of **1-NP** and **2-NP** (Tables S3 and S4, ESI†). Dimer 1 ($E^{SAPT(0)}$ = −95.03 kJ mol$^{-1}$) of **1-NP** and Dimer 2

[a] *School of Chemistry, Indian Institute of Science Education and Research Thiruvananthapuram, Maruthamala P.O., Vithura, Thiruvananthapuram, Kerala 695551, India. E-mail: mahesh@iisertvm.ac.in*
[b] *School of Physics, Indian Institute of Science Education and Research Thiruvananthapuram, Maruthamala P.O., Vithura, Thiruvananthapuram, Kerala 695551, India*

† Electronic supplementary information (ESI) available. CCDC 2389910 and 2389912. For ESI and crystallographic data in CIF or other electronic format see DOI: https://doi.org/10.1039/d4cc05351f

‡ These authors contributed equally.

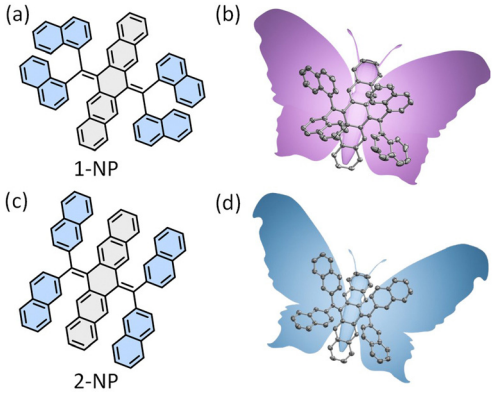


Fig. 1 Chemical structures of (a) **1-NP** and (c) **2-NP** and the crystal structures of (b) **1-NP** and (d) **2-NP**. Hydrogen atoms are omitted for clarity.

($E^{SAPT(0)}$ = −60.11 kJ mol$^{-1}$) of **2-NP** were identified as more stable compared to other identified dimers. The electrostatic surface potential (ESP) analysis provided a qualitative picture of electron density distribution in the crystalline geometry. The blue regions signify σ-hole having a positive potential, concentrated in the naphthalene fragments, whereas the red regions signify the electron-rich regions having a net negative potential, concentrated in the dihydropentacene core, validating the existence of a σ-hole···π interaction mediated herringbone motif (Fig. S12 and S13, ESI†).

Having elucidated the noncovalent interactions orchestrating the assembly of the crystal systems, we set out to explore the excitonic interactions prevalent in **1-NP** and **2-NP**. The excitonic coupling between the selected dimers were computed considering both the long-range coulombic ($J_{coul}$) and short-range charge transfer coupling ($J_{CT}$). $J_{coul}$ calculated using electronic energy transfer (EET) analysis revealed a low magnitude of $J_{coul}$ ($\leq$11.09 cm$^{-1}$) for all the identified dimers of **1-NP** and **2-NP** (Table S5, ESI†). Similarly, $J_{CT}$ computed using charge transfer integral package (CATNIP), also exhibited low magnitude of $J_{CT}$ ($\leq$13.63 cm$^{-1}$). Insights into the charge transport properties in the crystal systems were obtained by analyzing the anisotropic charge carrier mobility.[17,18] Higher hole mobility was observed in both **1-NP** and **2-NP** with its maxima around the 30°–210° axis ($\mu_h$ = 0.293 cm$^2$ V$^{-1}$ s$^{-1}$ for **1-NP** and $\mu_h$ = 0.928 cm$^2$ V$^{-1}$ s$^{-1}$ for **2-NP**) with respect to the conducting channel. An ambipolar character of **1-NP** crystals could be visualized, whereas in **2-NP**, the hole mobility is considerably higher compared to electron mobility (Fig. S14 and S15, ESI†).

Spectroscopic inspections for **1-NP** and **2-NP** were performed to comprehend distinct luminescence properties at the solution state and crystalline state. In the solution state, the electronic absorption spectra recorded for **1-NP** and **2-NP** in hexane exhibited maxima at 217 and 221 nm, respectively (Fig. S16, ESI†). The Kubelka–Munk absorbance of **1-NP** and **2-NP** crystals revealed broad spectra spanning from ~200–410 nm for **1-NP** and ~200–500 nm for **2-NP** (Fig. S17, ESI†). Notably, the absorption spectra of **1-NP** and **2-NP** crystals exhibited a red shift compared to their solution-state spectra. Solvent-dependent absorption spectra of **1-NP** and **2-NP** were

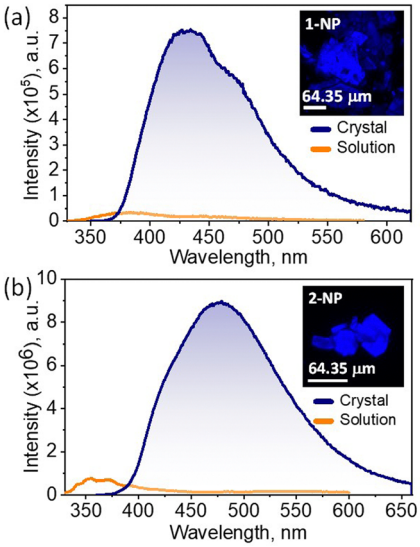


Fig. 2 Fluorescence spectra of (a) **1-NP** and (b) **2-NP** in tetrahydrofuran solution (10 μM, orange line) and crystalline state (blue line). Inset showing the confocal images of the respective crystals.

recorded in hexane, tetrahydrofuran (THF), and acetonitrile solution (Fig. S18, ESI†). The spectra obtained revealed negligible solvatochromism in both **1-NP** and **2-NP**. The emission spectra of **1-NP** and **2-NP**, recorded by exciting at 310 nm, exhibited weak emission bands having maxima at 382 and 355 nm, respectively (Fig. 2 and Fig. S19, ESI†). The fluorescence quantum yield measurements of **1-NP** and **2-NP** in THF solution relative to quinine sulphate in water resulted in <1% yield, establishing its weak emissive nature. The fluorescence emission spectra of **1-NP** and **2-NP** crystals were recorded by exciting the crystals at 340 nm. Interestingly, **1-NP** exhibited broad intense emission spectra in the range ~364–660 nm with a maximum of 430 nm, and **2-NP** exhibited fluorescence spectra ranging from ~374–660 nm with a maximum of 479 nm (Fig. 2). The photoluminescence quantum yield of the crystals was recorded by absolute method, unambiguously confirming the enhancement in the solid-state luminescence in **1-NP** ($\phi_{PL}$ = 22.3%) and **2-NP** ($\phi_{PL}$ = 9.4%) crystals. The excitation spectra of the **1-NP** and **2-NP** crystals revealed maxima at 334 and 379 nm, respectively (Fig. S20a, ESI†). The time-resolved fluorescence decay profiles of crystalline samples were acquired by exciting the sample at 314 nm. The fluorescence decay profile of **1-NP** and **2-NP** revealed a mono-exponential decay with a fluorescence lifetime of 2.52 ns and 2.38 ns, respectively (Fig. S20b, ESI†).

In a bid to understand the aggregation-induced photophysical characteristics, the emission spectra of **1-NP** and **2-NP** (0.1 mM in THF) were recorded in THF:$H_2O$ solvent mixtures. Initially, low fluorescence intensity was observed in THF solution which intensified upon continued increase of $H_2O$ fraction ($f_w$) (Fig. S21a, ESI†). In **1-NP**, an increased emission intensity accompanied by the gradual red-shifted maximum in the ~450–475 nm range ($f_w$ < 70%) was observed. The formation of a long wavelength band dominated in $f_w$ > 80%,

 

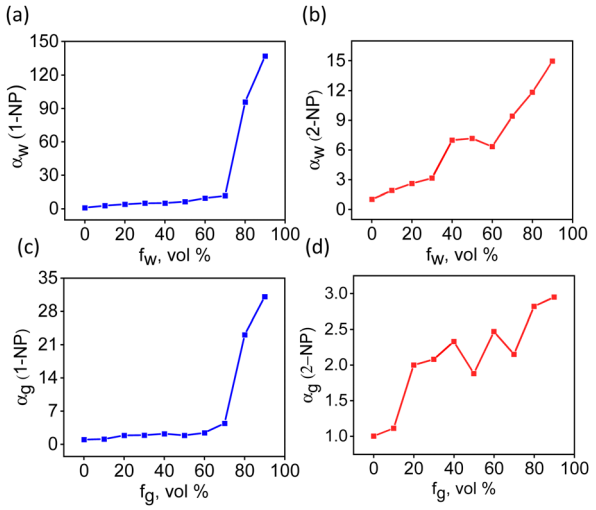


Fig. 3 Relative fluorescence intensity $\alpha_w$ of (a) **1-NP** and (b) **2-NP** in THF:water mixtures at different water fractions, $f_w$ ($\alpha_w = I/I_0$, $I_0$: Intensity at $f_w$ = 0%). Relative fluorescence intensity $\alpha_g$ of (c) **1-NP** and (d) **2-NP** in methanol: glycerol mixtures at different glycerol fractions, $f_g$ ($\alpha_g = I/I_0$, $I_0$: Intensity at $f_g$ = 0%).

notably 90% $H_2O$ mixture exhibited 137-fold increase from the initial intensity ($I_0$) with a broad emission maximum in the 570 nm range (Fig. 3a). For **2-NP**, the intrinsic emission in the 350 nm range was prominent in lower $f_w$ (<40%) which then gradually started to diminish as $f_w$ increased (Fig. S21b and S22, ESI†). The presence of a broad red-shifted band started to emerge, having maximum at 480 nm till $f_w$ reached 60%, after which the band at 530 nm started to dominate, with 90% $f_w$ showing 16-fold increase with respect to $I_0$ (Fig. 3b and Fig. S21b, ESI†). The presence of broad red-shifted emission, which intensified upon increasing $f_w$, could indicate the possibility of intra- and/or inter-molecular TSC enhanced by the formation of amorphous aggregates having low π···π interaction in both **1-NP** and **2-NP**.[12] The excitation-dependent emission spectra of 1 mM **1-NP** and **2-NP** in THF revealed negligible excitation wavelength dependence (Fig. S23, ESI†). The emission spectra of **1-NP** and **2-NP** (10 μM) were recorded in frozen THF solvent, excluding the possibility of bond rotations. The spectra obtained exhibited trends in line with TSC-mediated emission with negligible excitation wavelength dependence (Fig. S24, ESI†). Hinting at the dominant role of intramolecular TSC in governing aggregate state photophysics.[9]

To unveil the mechanism of enhanced emission in the crystalline and aggregate state, viscosity-dependent measurements were performed in methanol:glycerol mixture. **1-NP** and **2-NP** demonstrated a significant rise in emission as the glycerol fraction ($f_g$) increased. Notably, at 90% $f_g$ **1-NP** and **2-NP** exhibited 93-fold and 16-fold enhancement in $\alpha_g$ respectively, compared to the initial intensity (Fig. 3c, d and Fig. S25, ESI†). The time-resolved fluorescence decay profile of **1-NP** and **2-NP** at 95% and 50% $f_g$, were recorded by exciting at 310 nm. In an equal proportion of methanol and glycerol ($f_g$ = 50%), **1-NP** and **2-NP** exhibited mono-exponential decay with fluorescence lifetime of 3.15 and 2.86 ns, respectively (Fig. S26, ESI†). Interestingly, 95% $f_g$ exhibited an enhancement in fluorescence lifetime with $\tau_{avg}$ = 3.17 for **1-NP** and $\tau_{avg}$ = 3.38 ns for **2-NP** (Table S6, ESI†). The rise in viscosity restricts the bond rotations possible at the molecular level, explaining the enhanced fluorescence lifetime in higher $f_g$. This suggests that the RIM is a possible mechanism for the enhancement of emission in the crystalline state of **1-NP** and **2-NP**.

To decipher the origin of boosted luminescence at the crystalline/aggregate state of **1-NP** and **2-NP**, calculations were performed at the minimum energy geometries of the ground state ($S_0$), excited singlet ($S_1$) and triplet ($T_1$) states employing density functional theory (DFT). The excited state frontier molecular orbitals obtained from the optimised $S_1$ geometries of **1-NP** and **2-NP** exhibited through space orbital overlap, indicating the presence of TSC (Fig. 4a and Fig. S27, ESI†). The $S_1$ state geometries of **1-NP** and **2-NP** displayed increased

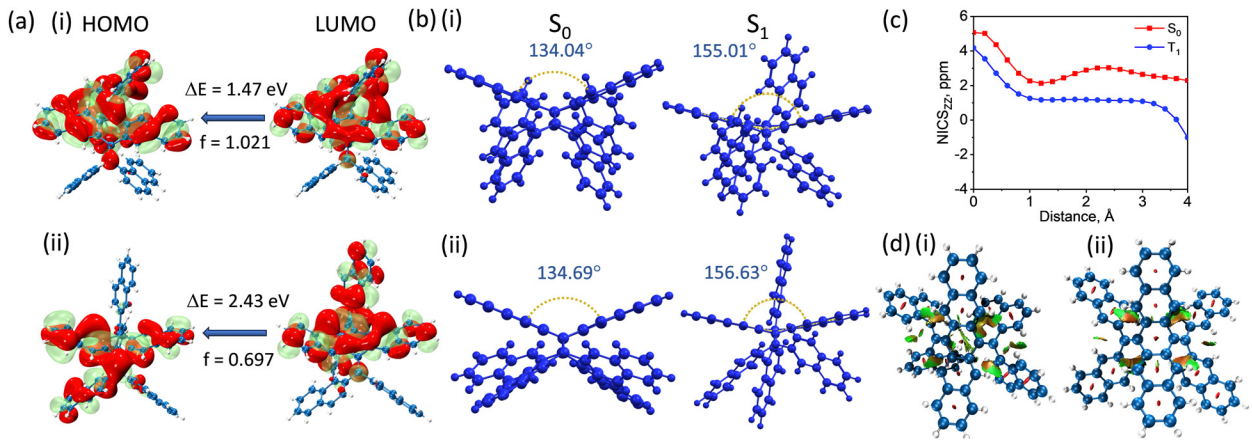


Fig. 4 (a) Excited singlet state ($S_1$) frontier molecular orbitals of (i) **1-NP** and (ii) **2-NP** exhibiting through space orbital overlap, with the calculated HOMO–LUMO energy gap ($\Delta E$) and corresponding oscillatory strength ($f$). (b) Optimized ground state ($S_0$) and first singlet excited state ($S_1$) state of (i) **1-NP** and (ii) **2-NP** showing the excited state planarization. (c) $NICS_{ZZ}$ scan of **1-NP** in $S_0$ and first triplet excited state ($T_1$) states. (d) NCI plots of (i) **1-NP** and (ii) **2-NP**.

planarity compared to $S_0$, indicated by increase in the angle between the terminal rings from 133.97° to 155.01° for **1-NP** and 128.47° to 156.63° for **2-NP** (Fig. 4b and Fig. S28, S29, ESI†). This conformation formed by the internal conversion of the Frank–Condon excited state will be lower in energy, and opens up various non-radiative pathways, leading to weak emission in the solution state. The planarization of $S_1$ geometry in similar molecules reduces the antiaromatic character, explaining the lowered energy level from the Frank–Condon state.[13] Nucleus-independent chemical shift ($NICS_{ZZ}$) scan revealed antiaromaticity relief from the ground state geometry to the triplet state geometry (Fig. 4c, Fig. S30 and Tables S7, S8, ESI†).[19] This possibly opens up a new nonradiative pathway where the planarized $S_1$ state geometry can facilitate intersystem crossing. However, in the crystalline state, the planarization of $S_1$ state geometry *via* internal conversion is inhibited due to the interaction between neighbouring molecules. Hence, the excited molecule reaches the ground state radiatively, possibly explaining the luminescence enhancement in the crystalline states of **1-NP** and **2-NP**. The presence of TSC between the core and naphthalene moieties was further validated by the stabilizing green iso-surface obtained from NCI analysis for the monomers (Fig. 4d).

To gain further insights into the photophysical properties at the aggregate state, the role of inter- and intra-molecular interactions was analyzed. The negligible proportion of C···C interactions obtained from Hirshfeld analysis, along with the low magnitude of excitonic coupling obtained for all the identified dimers, corroborated the dominant role of intramolecular rather than intermolecular interactions in governing the aggregate state photophysics. The inherent cross-conjugated nature of **1-NP** and **2-NP** diminishes the extent of TBC, further validated by the anisotropy of the induced current density (AICD) plots. The opposing current densities at the central six-membered ring indicate the disruption of continuous delocalization of π-electrons within the chromophore, thereby reducing TBC (Fig. S31, ESI†). Further inspection of the crystal structure of both the isomers revealed the possibility of TSC evident from the C···C distance of $<3.4$ Å (Fig. S32, ESI†). Insights into the charge delocalisation were obtained using fragment-based TheoDORE analysis where partial CT nature was identified for both **1-NP** (CT = 0.328) and for **2-NP** (CT = 0.363), which implies the partial delocalisation of hole and electron densities across the fragments, predominantly *via* TSC (Tables S9, S10 and Fig. S33, S34, ESI†).[20] Further validation was obtained from the hole–electron analysis, which elucidated the spatial electron overlap between the core and naphthalene moieties (Fig. S35, ESI†). Hence formation of aggregates restricts the motion of the naphthalene fragments, thereby enhancing the intramolecular interactions governing TSC, ultimately leading to enhanced emission in the long wavelength region.[9]

In summary, TSC-assisted luminescence enhancement is reported in two butterfly-like architectures of tetra-naphthalene connected dihydropentacene derivatives, **1-NP** and **2-NP**. Spectroscopic investigations revealed the presence of AIE, where broad, intense PL spectra were observed for both crystals ($\phi_{PL}$ = 22.3% for **1-NP** and $\phi_{PL}$ = 9.4%) in contrast to the weakly emissive monomeric solution ($\phi_{PL} < 1\%$). Tuning the bond rotation and intermolecular proximity of molecules using appropriate solvent mixtures further validated the AIE mechanisms. Enhanced luminescence was observed upon increasing the solvent viscosity, indicating the significance of RIM mechanisms. Hirshfeld surface, NCI, and FMO analysis in the $S_1$ state elucidated the possible existence of intramolecular TSC in the chromophores, resulting in the emergence of a red-shifted intense PL band in the crystalline state and aggregate state.

M. H. acknowledges MoE-STARS/STARS-2/2023-0770 for financial support. S. S. acknowledges PMRF for financial assistance. A. H. acknowledges DST-INSPIRE for financial assistance. We thank Dr. Lijina M. P. for assistance in the synthesis. We kindly thank Prof. Babu Varghese and Mr Alex P. Andrews for their assistance in X-ray diffraction analyses and refinement. We thank the Padmanabha HPC cluster at IISER TVM for the computing time.

## Data availability

All the experimental data were provided in the ESI.†

## Conflicts of interest

There are no conflicts to declare.

## References

1 O. Ostroverkhova, *Chem. Rev.*, 2016, **116**, 13279–13412.
2 L. Basabe-Desmonts, D. N. Reinhoudt and M. Crego-Calama, *Chem. Soc. Rev.*, 2007, **36**, 993–1017.
3 C. Zhu, R. T. K. Kwok, J. W. Y. Lam and B. Z. Tang, *ACS Appl. Bio. Mater.*, 2018, **1**, 1768–1786.
4 J. Mei, N. L. C. Leung, R. T. K. Kwok, J. W. Y. Lam and B. Z. Tang, *Chem. Rev.*, 2015, **115**, 11718.
5 A. R. Mallia, R. Sethy, V. Bhat and M. Hariharan, *J. Mater. Chem. C*, 2016, **4**, 2931–2935.
6 J. Luo, Z. Xie, J. W. Y. Lam, L. Cheng, H. Chen, C. Qiu, H. S. Kwok, X. Zhan, Y. Liu, D. Zhu and B. Z. Tang, *Chem. Commun.*, 2001, 1740.
7 R. Hoffmann, *Acc. Chem. Res.*, 1971, **4**, 1–9.
8 Y. Hong, J. W. Y. Lam and B. Z. Tang, *Chem. Commun.*, 2009, 4332–4353.
9 Q. Xu, J. Zhang, J. Z. Sun, H. Zhang and B. Z. Tang, *Nat. Photon.*, 2024, **18**, 1185–1194.
10 P. Shen, Z. Zhuang, X.-F. Jiang, J. Li, S. Yao, Z. Zhao and B. Z. Tang, *J. Phys. Chem. Lett.*, 2019, **10**, 2648–2656.
11 S. Tang, T. Yang, Z. Zhao, T. Zhu, Q. Zhang, W. Hou and W. Z. Yuan, *Chem. Soc. Rev.*, 2021, **50**, 12616–12655.
12 Y. Wang, J. Zhang, Q. Xu, W. Tu, L. Wang, Y. Xie, J. Z. Sun, F. Huang, H. Zhang and B. Z. Tang, *Nat. Commun.*, 2024, **15**, 6426.
13 X. Yin, J. Z. Low, K. J. Fallon, D. W. Paley and L. M. Campos, *Chem. Sci.*, 2019, **10**, 10733–10739.
14 S. Kumar and Y.-T. Tao, *Org. Lett.*, 2018, **20**, 2320–2323.
15 M. A. Spackman and D. Jayatilaka, *CrystEngComm*, 2009, **11**, 19–32.
16 B. Jeziorski, R. Moszynski and K. Szalewicz, *Chem. Rev.*, 1994, **94**, 1887–1930.
17 W.-Q. Deng, L. Sun, J.-D. Huang, S. Chai, S.-H. Wen and K.-L. Han, *Nat. Protoc.*, 2015, **10**, 632–642.
18 V. Bhat, G. Gopan, N. G. Nair and M. Hariharan, *Chem. – Eur. J.*, 2018, **24**, 8679–8685.
19 A. Stanger, *J. Org. Chem.*, 2006, **71**, 883–893.
20 F. Plasser, *J. Chem. Phys.*, 2020, 152.

 